Effect of Sliding Conditions on Micropitting Behaviour of AISI 304 Stainless Steel in Chloride Containing Solution

Y. Sun*, R. Bailey

School of Engineering and Sustainable Development
Faculty of Technology
De Montfort University
Leicester LE1 9BH, UK

* Corresponding author: Email: ysun01@dmu.ac.uk; Tel: (44) 116 2577072

ABSTRACT

The tribo-electrochemical behaviour of AISI 304 austenitic stainless steel in 0.5 M NaCl solution is investigated at an anodic potential of 70 mV(SCE) under controlled sliding and electrochemical conditions. It is found that at such an anodic potential where corrosion pits do not form without sliding, numerous micro-pits are found inside the sliding tracks under certain sliding conditions. There exists a critical combination of frequency, load and sliding duration for the development of the pits. The results are discussed considering the accumulation of mechanical damages induced by sliding and the competition between wear and pit growth during the process.

Keywords: Stainless steel; Pitting corrosion; Potentiostatic; Sliding wear; Tribocorrosion

1. Introduction

Stainless steels find wide applications in industry because they have good corrosion resistance and mechanical strength and are of low costs [1-3]. The corrosion resistance of this type of materials is believed to be associated with the existence of a stable oxide film on the surface, which is rich in chromium [4, 5]. This thin film makes the steel surface passive in many environments. In environments containing chlorides, however, stainless steels can experience pitting corrosion, which is believed to result from breakdown of the passive film in localised areas containing sulphur-rich inclusions [6]. The localised breakdown of passivity leads to pit initiation and formation of metastable pits which can develop into stable pits at potentials above a critical potential (i.e. pitting potential) or at temperatures higher than the pitting temperature [7]. Thus, below the pitting potential stainless steels are not expected to suffer from pitting corrosion.

In many practical applications, stainless steel components are subjected to mechanical actions such as sliding, rolling and rolling-sliding contact motions in corrosive environments such as in artificial hip joints, pumps and valves. Breakdown of the passive film during wear processes can increase metal dissolution. Mechanical wear may also be accelerated due to increased metal dissolution. This is the phenomenon of tribocorrosion, which has been increasingly studied during the past two decades [8-11]. These studies have identified the complex phenomena involved and the effect of wear on the electrochemical response of materials. The synergy between corrosion and wear has been confirmed and quantified through modelling [9]. In particular, the mechanical wear actions can destruct the oxide film in the areas that make real contact, and thus can accelerate localised corrosion, i.e. pitting corrosion. In a recent study [12], it was found that when 304 austenitic stainless steel was sliding against an alumina slider in a solution containing NaCl, numerous micron-sized corrosion pits could be formed in the sliding track even when the applied potentials were well below the pitting

potential. The formation of corrosion pits must be related to the mechanical sliding actions and is expected to be affected by the sliding conditions.

This work aims to investigate the effect of sliding conditions on the micropitting behaviour of AISI 304 steel in a chloride-containing solution under unidirectional sliding at an anodic potential where pitting corrosion is normally not expected. Several sets of experiments were systematically conducted, including anodic polarisation measurements during sliding and potentiostatic measurements at a fixed anodic potential under different sliding conditions, such as contact frequency, load and time. The results are discussed considering the role of the accumulation of mechanical damages in micropit formation.

2. Experimental procedures

The test material used was AISI 304 austenitic stainless steel, the composition of which are listed below (in wt%): 0.07C, 18.51Cr, 9.42Ni, 2.12Mn and Fe. The hardness of the steel was 205 $HV_{0.1}$. The as-received plate was cut into 20 x 20 x 2.5 mm^3 sizes specimens. Before tribo-electrochemical test, the specimens were prepared by grinding using SiC grinding papers and then by polishing such that a smooth surface finish of 0.03 μm (R_a) was achieved. After ultra-sonication for 5 min in ethanol, the specimen was loaded into the test cell, with a test area of 1.4 x 1.4 cm^2 open to the solution. Other areas of the specimen were masked by using an insulating tape.

The tribo-electrochemical system was the same as that reported in [12, 13] and is illustrated in Fig. 1. A pin-on-disk tribometer and a potentiostat (ACM Gill AC) were integrated to facilitate the simultaneous measurements of friction, wear and electrochemical potential and current. The test cell and fixtures were made of nylon and the slider was an 8 mm diameter alumina ball supplied by Trafalgar Bearings Ltd, which had nominal hardness of 1700 HV, Young's modulus of 303 GPa and surface finish of 0.02 μm (R_a). This setup was necessary to

make sure that electrochemical reactions only occur in the test area of the specimen. When the specimen rotated against the alumina slider in the test electrolyte, a circular sliding track of 6 mm diameter was produced.

0.5 M NaCl in double distilled water was used as the electrolyte in the test cell of 60 ml capacity. The specimen immersed in the solution was the working electrode, the potential of which was measured using a saturated calomel electrode (SCE) as the reference electrode. To measure the electric current, a platinum foil served as the counter electrode (see Fig. 1). All tests were conducted in ambient atmosphere and at room temperature (22ºC). Every test was conducted twice and the results were found to be consistent and reproducible.

Four sets of measurements were carried out in this work. First, potentiodynamic tests were done to measure the anodic polarisation behaviour of the specimens. These tests were implemented both without sliding and with sliding on. The potential was scanned anodically at 1 mV s^{-1} from -200 mV(SCE) vs OCP until 1000 mV(SCE) vs OCP. During the test, the specimen was rotating at 120 rpm (2 Hz frequency) either without contact (no sliding) or with contact (sliding) with the slider at a 10 N contact load. Before the test, the specimen was allowed to rest at open circuit potential (OCP) for 600 s.

Based on the results of the anodic polarisation measurements, the next three series of experiments were done potentiostatically at an anodic potential of 70 mV(SCE), which was well below the pitting potential of the investigated steel under the condition without sliding. First, the effect of contact frequency was investigated by varying the frequency from 0.33 Hz to 4 Hz, while keeping the total number of sliding cycles (3600) and contact load (10 N) unchanged for each test. Second, the effect of sliding duration was investigated at the fixed 2 Hz contact frequency and 10 N load, by varying the sliding time from 300 s to 7200 s. Third, the effect of load was investigated at a fixed contact frequency of 2 Hz and total number of sliding cycles of 3600, by varying the load from 1 N to 20 N. This load range corresponds to

maximum Hertzian contact pressures ranging from 460 MPa to 1270 MPa during initial contact. For each test, the specimen was allowed to rest for 600 s at the polarisation potential (70 mV(SCE)) before sliding started, and after completion of sliding, the specimen was continuously polarised at 70 mV(SCE) for further 600 s. This test setup allowed for the continuous recording of the current transient during the whole measurement process.

The sliding track surface profiles at several locations were measured using a stylus surface profilometer. This allowed for the evaluation of the sliding track cross-sectional area and the total material loss (TML) in volume. The sliding track surfaces were examined microscopically using optical and scanning electron microscopes (SEM), as well as atomic force microscope (AFM). The optical microscope used was the Nikon Eclipse LV150N, which has the extended depth of focus function with the help of a motorised stage allowing for the automatic focus at various depths. This allows for the generation of a three dimension (3D) image within the focus range.

3. Experimental Results

3.1 Potentiodynamic polarisation curves

Fig. 2 shows the anodic polarisation curves measured at 2 Hz contact frequency and under 10 N contact load. The polarisation curve measured without sliding was typical of stainless steel and was characterised by a passive region, where the current density gradually became levelling-off. At the potential about 500 mV(SCE), pitting corrosion occurred, leading to a quick rise in current density [12]. With sliding on, the corrosion potential of the specimen was shifted negatively by more than 200 mV(SCE). This suggests that the passive state of the sliding surface was destructed by the mechanical action [14-18]. More noticeably, during the sliding period, the current density was increased considerably (Fig. 2) and there was no passive region because the current density continuously increased to reach a high value more than 1

mA cm^{-2}, which was considerably higher than that recorded without sliding in the passive region (10^{-3} mA cm^{-2}). This current increase can be accounted for by the activation of the sliding track area during sliding. Fig. 3 shows the morphology of the sliding track after the potentiodynamic test. The sliding track was populated with many corrosion pits of microscopic scale, mostly less than 15 μm in diameter. It is also interesting to note from Fig. 2 that the current density during sliding did not experience an abrupt rise. Micropit formation was clearly dominant in the sliding track and led to the observed increase in current density.

After measuring the polarisation curves, further experiments were implemented potentiostatically at a fixed anodic potential of 70 mV(SCE) to investigate the effect of contact frequency, sliding time and contact load on the micropitting behaviour of the steel. The chosen potential of 70 mV(SCE) was in the passive region and well below the pitting potential of the steel under the condition without sliding, as can be seen in Fig. 2. Thus no pitting corrosion should be expected at such a potential without sliding.

3.2 Effect of contact frequency

Fig. 4a shows the current transient curves recorded (at 70 mV(SCE)) at various contact frequencies for the same number of sliding cycles of 3600 and under the same contact load of 10 N. In agreement with many other observations for passive systems [14, 15, 17]**,** the current increased abruptly when sliding started and remained at a high level during the whole sliding period. Depassivation of the sliding track surface was responsible for such an accelerated metal dissolution, i.e. wear-induced corrosion [19, 20]. After the completion of sliding, the sliding track surface repassivated, as evidenced by the rapid decrease in current towards the low value registered before sliding [16, 21]. Although the recorded current during two repeated tests at some frequencies scattered quite noticeably, there was a general trend that the current during sliding increased with increasing contact frequency (Fig. 4a), i.e. the kinetics of metal dissolution increased with contact frequency. As contact frequency was increased, the time

interval between two subsequent contacts was reduced, thus there was less time for repassivation. Therefore, a higher contact frequency led to a more activated state in the sliding track. It should be pointed out that because the total number of sliding cycles at each frequency was fixed at 3600, in order to achieve the same number of sliding cycles, shorter times were required at higher frequencies. This means that the activated sliding tracks were exposed to the solution for shorter times at higher frequencies. The total charge evolved during the sliding period, i.e. the area enclosed by each current transient curve in Fig. 4a, is a better parameter to characterise the amount of metal dissolution or corrosion from the sliding track. Indeed, when the total material loss (TML) in volume from the sliding track was plotted against the total charge, a very consistent linear correlation was observed, as shown in Fig. 4b. This indicates the dominant role played by anodic dissolution in determining the material removal behaviour at the anodic potential. For comparison purpose, the TML produced at a cathodic potential of -900 mV(SCE) was also included in Fig. 4b. The TML at the cathodic potential did not vary significantly with contact frequency and was much smaller than those produced at the anodic potential of 70 mV(SCE). This agrees with previous results that the wear rate of stainless steel was increased when the electrochemical potential was increased from cathodic to anodic in chloride containing media [12,14].

Fig. 5a shows a typical three dimensional view of the sliding track produced during tribocorrosion under 10 N load and at 1 Hz frequency, together with the measured surface profile across the sliding track. Many parallel abrasion marks and micropits can be observed in the track which has a wear depth of about 6 μm. The values of TML presented in Fig. 4b were measured from the sliding track profiles. Fig. 5b shows the corresponding wear scar on counterface alumina ball. It can be seen that there were no significant damage and wear occurring to the ball.

Anodic dissolution in the sliding track mostly occurred through micropitting corrosion, see Fig. 6. However, the presence, number and size of pits depended on contact frequency. At the lowest frequency of 0.33 Hz, only a very small number of micro-pits, smaller than 5 μm in size, were observed. With increasing contact frequency up to 3 Hz, the number and size of pits were increased, so much so that the sliding tracks produced at the frequencies of 1, 2 and 3 Hz were populated with a large number of micro-pits of varying sizes, mostly less than 15 μm in diameter. Interestingly, when the contact frequency was further increased to 4 Hz, almost no pits were found in the sliding track. Instead, many abrasion marks were found, together with severe plastic deformation and material pileup at the edges.

3.3 Effect of sliding time

Fig. 7a shows the current transient curves recorded at 70 mV(SCE) for various sliding times at a fixed 2 Hz frequency and under a constant 10 N load. The curves obtained from individual tests almost overlap with one another during the common sliding periods, confirming the consistency of test results in this work. In Fig. 7b, the measured TML was plotted against sliding time, showing a linear relationship. When the TML was plotted against total charge evolved during sliding, a linear relationship was also obtained (not shown). Again, this indicates the dominant role of anodic dissolution in the tribo-electrochemcal process.

The morphologies of the sliding tracks produced for various sliding times are shown in Fig. 8. After sliding for 300 s, which corresponds to 600 sliding cycles, almost no visible pits were present in the sliding track. When the sliding time was increased to 720 s, some micropits started to appear in the sliding track. The number and size of micropits increased with increasing sliding time up to 1800 s. Again, most of the pits were less than 15 μm in size. Interestingly, when the sliding time was further increased to 3000 s, the number of pits decreased, particularly at the centre of the sliding track, where almost no pits were visible and there were deep and wide abrasion marks due to accelerated mechanical wear. After an

extended sliding time of 7200 s, the sliding track was completely populated with deep and wide abrasion marks with very few visible pits, and material pile-up at the track edges became more obvious. Clearly, the presence of micropits inside the sliding track was time-dependent. There appeared an incubation time for the micropits to develop in the sliding track. The number of pits increased with increasing sliding time; but when severe abrasion and plastic deformation occurred in the sliding track, the micropits were removed rapidly such that the rough wear track surface became nearly free from pits.

3.4 Effect of contact load

Further tests were conducted under various contact loads at a fixed frequency of 2 Hz for a total duration of 1800 s (3600 sliding cycles). The resultant current transient curves are given in Fig. 9a, which clearly show that the current evolved during the sliding period increased with contact load. Under contact loads below 10 N, the current was quite stable during the sliding period. Under higher loads, the current became less stable and fluctuated during the sliding period. Fig. 9b shows the variation of TML with total charge produced at various contact loads. Clearly, the TML increased with load and total charge. However, the relationship between TML and total charge was no longer linear, demonstrating the increased contribution of mechanical wear to TML with increasing contact load.

Microscopic examination (Fig. 10) showed that the sliding track produced under 1 N load was free from corrosion pits. Under 2 N load, a few micropits could be observed inside the sliding track. Micropitting was more evident inside the sliding track produced under 4 N load and became very significant under the load of 10 N. After increasing the contact load to 15 N, the number of micropits was reduced at the central region of the sliding track, which was populated with deep and wide abrasion marks due to increased plastic deformation and mechanical wear. Under a further higher load of 20 N, almost no pits were observed, instead, the sliding track was abraded severely by the alumina slider, which induced severe plastic

deformation and led to material pile-up. Clearly, there existed a critical load for the micropits to develop in the sliding track. The number of pits increased with increasing load, but when severe mechanical wear occurred at high loads, the micropits were removed rapidly such that the rough wear track surface became nearly free from pits.

4. Discussion

The results presented in section 3 demonstrated that at an anodic potential which is well below the pitting potential, micropits can be formed in the sliding track during sliding in the NaCl containing solution. These micropits were metastable because after the completion of sliding, these pits did not grow in size even when the specimens were polarised at 70 mV(SCE) for further 600 s. The metastablity of the pits was confirmed by the rapid decrease of the current after the termination of sliding (Figs 4a, 7a and 9a). This fact suggests that the micro corrosion pits were formed under the mechanical actions of the slider and died in the absence of sliding. This agrees with the observation in [22] regarding the erosion-corrosion of 304L stainless steel. Indeed, this work clearly showed that the presence, number and size of micropits depended very much on the mechanical sliding conditions, i.e. contact frequency, load and sliding time. A consistent observation was that corrosion pits could be formed only when the contact frequency was sufficiently high, contact load was sufficiently large and sliding time was sufficiently long. However, at excessively high frequencies and loads, as well as after prolonged sliding, the corrosion pits may disappear from the sliding track, as can be clearly seen from Figs 6, 8 and 10. Such behaviour could be related to the accumulation of mechanical damages, the evolution of surface roughness and pit growth and material removal by wear, as elaborated more in the following paragraphs.

It has been well recognised that pitting corrosion of metals in environments containing chlorides involves three stages, i.e. passive film breakdown in localised areas, metastable pit

formation and stable pit growth [23-28]. The rate of pit growth is believed to be dominated by the diffusion of metal ions from the solution inside the pit to the solution outside the pit [27-30]. For a pit to grow in size, an aggressive pit solution must be maintained [27, 30]. Thus, a certain diffusion barrier is required at the pit mouth to prevent the pit anolyte from being diluted with the external electrolyte. Such a diffusion barrier can be in the form of a cover over the pit mouth in the metastable stage [27, 31]. The metastable pit can become stable if the pit is deep enough to serve as a diffusion barrier. It is envisaged that metastable pit growth and pit metastability to stability transition are rendered easier if metal dissolution is accelerated at the pit and the pit initiation sites are more occluded or less open. These are the conditions that prevail during the sliding process. The effect of sliding on pit formation at potentials below the pitting potential can thus be considered as follows.

Firstly, local breakdown of passivity becomes much easier during sliding because sliding can destruct the oxide film from the real contact areas inside the sliding track, thus providing the activated sites for pit initiation. In particular, sliding induces severe plastic deformation, increases crystal lattice energy and dislocation densities in the real contact areas and thus can accelerate metal dissolution in the pit initiation sites [32, 33]. These would lead to rapid pit growth even at low potentials.

Secondly, sliding induces the formation of microcracks or voids, shearing and delamination of materials, which are occluded sites favouring pit development. Many of the pits are thought to be formed at such sites, as can be seen from Fig. 3. An example is given in Fig. 11a, which is an AFM image showing the collapse of the surface material into an underneath pit. The pit seems to have formed at the surface and developed beneath the surface material. Further sliding contact in the pit area led to the collapsing of the material into the pit. To further demonstrate this, a cross sectional specimen was prepared from the sample tested at 1Hz and 10 N load and the subsurface was examined microscopically, see Fig. 12. It can be

seen that in addition to the shallow pits formed at the surface, some pits developed below the surface to a depth of several microns leading the collapse of the surface material.

Thirdly, sliding increases the surface roughness of the wear track due to plastic deformation, material delamination and abrasion. It has been proven that a roughened surface provides more occluded sites favouring the development of pits at lower potentials [31]. The scratches became less-open areas due to the plastic deformation and smearing of materials at surrounding regions, and thus provided diffusion barriers to favour the development of corrosion pits.

It is important to note that sliding may also have an adverse effect on pit growth, because sliding can remove pit covers and other diffusion barriers from the pit mouth, leading to the death and repassivation of the pits and the reduction in pit size and depth or even complete removal of the pits. This can be clearly seen in Fig. 11b, which is an AFM image showing a shallow micropit with the cover removed by the sliding actions. The pit seemed to have been repassivated and failed to grow in size. This explains the variation of pit size and the microscopic nature of the pits inside the sliding track. Fig. 11c shows an AFM 2D image of a micro-pit and a topography scan across the pit. From the depth profile shown in Fig. 11d, it is clear that the depth of the pit is less than 150 nm. Fig 13 shows a three dimensional view of some micropits, together with the sectional view of one of the relatively large pit to show the morphology of the pit below the surface. Some of the pits can be as deep as 2 to 3 microns and have a conical shape below the surface.

From the above discussion, it can be deduced that mechanical damages and occluded or less-open sites must be created during the sliding process in order for micropits to develop and survive some sliding cycles at anodic potentials below the pitting potential. Thus a sufficient combination of load, sliding time and contact frequency is required to induce such mechanical damages as accumulation of plastic deformation, micro-cracking and surface roughening. This

agrees with the experimental results that almost no corrosion pits were observed if the frequency was very low (0.33 Hz, Fig. 6), the load was not sufficiently high (1 N, Fig. 10) and the sliding duration was too short (300 s, Fig. 8). As the frequency, load and sliding time increased, the mechanical damages were also increased, leading to increased pit size and number of pits. However, the pit size was limited due to material removal by the wearing action, and when the material removal rate by wear exceeded the pit growth rate, the growing pits would be removed after a certain number of sliding cycles, such that very few pits would be left in the sliding track, as observed at the frequency of 4 Hz (Fig. 6), contact load of 20 N (Fig. 10) and after extended sliding for 7200 s (Fig. 8).

It should also be noted that the formation of pits could accelerate mechanical wear because the micropits can promote stress concentration and crack propagation [12, 34]. The dominant role of anodic dissolution in total material removal is demonstrated in Figs 4 and 9, which show the positive correlation between TML and total charge. The contributions of wear-accelerated corrosion and corrosion-accelerated wear to total material removal by tribocorrosion have been discussed by several investigators [12, 15, 20, 21, 34] and will not be discussed further here.

5. Conclusions

(1) Sliding leads to increased anodic currents in the NaCl solution and such a current increment increases with increasing contact frequency and load.

(2) Under certain conditions, sliding can promote micropit formation in the sliding track at anodic potentials lower than the pitting potential.

(3) The presence, number and size of micropits depend on sliding conditions. Generally, the number and size of corrosion pits increase with increasing contact frequency, load and sliding time. But at excessively high frequencies and loads and after prolonged sliding, the micropits may disappear due to increased mechanical wear.

(4) There exists a critical combination of contact frequency, load and sliding time for the development of corrosion pits in the wear track. Micropits do not form under all sliding conditions. Below a certain critical frequency, load and time, corrosion pits fail to develop in the wear track. This is believed to be due to the requirement for the accumulation of mechanical damages such as plastic deformation, cracking and surface roughening which favour the formation and development of corrosion pits.

Data Availability

All research data supporting this publication are directly available within this publication.

References

[1] V. Karki, M. Singh, Investigation of corrosion mechanism in Type 304 stainless steel under different corrosive environments: A SIMS study, International Journal of Mass Spectrometry. 421 (2017) 51-60.

[2] Y. Peng, C. Chen, X. Li, J. Gong, Y. Jiang, Z. Liu, Effect of low-temperature surface carburization on stress corrosion cracking of AISI 304 austenitic stainless steel, Surface and Coatings Technology. 328 (2017) 420-427.

[3] R.K. Gupta, N. Birbilis, The influence of nanocrystalline structure and processing route on corrosion of stainless steel: A review, Corrosion Science. 92 (2015) 1-15.

[4] Z.B. Zheng, Y.G. Zheng, Effects of surface treatments on the corrosion and erosion-corrosion of 304 stainless steel in 3.5% NaCl solution, Corrosion Science. 112 (2016) 657-668.

[5] F.A. Almuaili, S.A. McDonald, P.J. Withers, A.B. Cook, D.L. Engelberg, Strain-induced reactivation of corrosion pits in austenitic stainless steel, Corrosion Science. 125 (2017) 12-19.

[6] I. Park, S. Lee, M. Kang, S. Lee, Y. Lee, Pitting corrosion behavior in advanced high strength steels, Journal of Alloys and Compounds. 619 (2015) 205-210.

[7] N. Ebrahimi, M. Momeni, A. Kosari, M. Zakeri, M.H. Moayed, A comparative study of critical pitting temperature (CPT) of stainless steels by electrochemical impedance spectroscopy (EIS), potentiodynamic and potentiostatic techniques, Corrosion Science. 59 (2012) 96-102.

[8] Y. Sun, P. Dearnley, B. Mallia, Response of duplex Cr(N)/S and Cr(C)/S coatings on 316L stainless steel to tribocorrosion in 0.89% NaCl solution under plastic contact conditions, J Biomed Mater Res Part B. 105 (2017) 1503-1513.

[9] E. Huttunen-Saarivirta, L. Kilpi, T.J. Hakala, L. Carpen, H. Ronkainen, Tribocorrosion study of martensitic and austenitic stainless steels in 0.01M NaCl solution, Tribology International. 95 (2016) 358-371.

[10] Y. Ye, Y. Wang, X. Ma, D. Zhang, L. Wang, X. Li, Tribocorrosion behaviors of multilayer PVD DLC coated 304L stainless steel in seawater, Diamond and Related Materials. 79 (2017) 70-78.

[11] Y. Sun, R. Bailey, Improvement in tribocorrosion behavior of 304 stainless steel by surface mechanical attrition treatment, Surface and Coatings Technology. 253 (2014) 284-291.

[12] Y. Sun, V. Rana, Tribocorrosion behaviour of AISI 304 stainless steel in 0.5M NaCl solution, Materials Chemistry and Physics. 129 (2011) 138-147.

[13] Y. Sun, E. Haruman, Effect of electrochemical potential on tribocorrosion behavior of low temperature plasma carburized 316L stainless steel in 1M H2SO4 solution, Surface and Coatings Technology. 205 (2011) 4280-4290.

[14] P. Henry, J. Takadoum, P. Berçot, Tribocorrosion of 316L stainless steel and TA6V4 alloy in H2SO4 media, Corrosion Science. 51 (2009) 1308-1314.

[15] S. Mischler, Triboelectrochemical techniques and interpretation methods in tribocorrosion: A comparative evaluation, Tribology International. 41 (2008) 573-583.

[16] P. Ponthiaux, F. Wenger, D. Drees, J.P. Celis, Electrochemical techniques for studying tribocorrosion processes, Wear. 256 (2004) 459-468.

[17] Y.N. Kok, R. Akid, P.E. Hovsepian, Tribocorrosion testing of stainless steel (SS) and PVD coated SS using a modified scanning reference electrode technique, Wear. 259 (2005) 1472-1481.

[18] S. Kumar, Sankara Narayanan, T S N, S. Ganesh Sundara Raman, S.K. Seshadri, Evaluation of fretting corrosion behaviour of CP-Ti for orthopaedic implant applications, Tribology International. 43 (2010) 1245-1252.

[19] S. Mischler, P. Ponthiaux, A round robin on combined electrochemical and friction tests on alumina/stainless steel contacts in sulphuric acid, Wear. 248 (2001) 211-225.

[20] S.W. Watson, F.J. Friedersdorf, B.W. Madsen, S.D. Cramer, Methods of measuring wear-corrosion synergism, Wear. 181-183 (1995) 476-484.

[21] D. Landolt, S. Mischler, M. Stemp, Electrochemical methods in tribocorrosion: a critical appraisal, Electrochimica Acta. 46 (2001) 3913-3929.

[22] G.T. Burstein, K. Sasaki, The birth of corrosion pits as stimulated by slurry erosion, Corrosion Science. 42 (2000) 841-860.

[23] Z. Szklarska-Smialowska, Pitting corrosion of metals, Illustrated ed., Nat. Assoc. of Corrosion Engineers, Houston, Tex, 1986.

[24] L.F. Garfias-Mesias, J.M. Sykes, Metastable pitting in 25 Cr duplex stainless steel, Corrosion Science. 41 (1999) 959-987.

[25] J.W. Schultze, M.M. Lohrengel, Stability, reactivity and breakdown of passive films. Problems of recent and future research, Electrochimica Acta. 45 (2000) 2499-2513.

[26] E. Sikora, D.D. Macdonald, Nature of the passive film on nickel, Electrochimica Acta. 48 (2002) 69-77.

[27] P.C. Pistorius, G.T. Burstein, Metastable pitting corrosion of stainless steel and the transition to stability, Philos Trans Phys Sci Eng. 341 (1992) 531-559.

[28] M.B. Ives, Metallography of pitting corrosion, Materials Characterization. 28 (1992) 257-270.

[29] G.O. Ilevbare, G.T. Burstein, The role of alloyed molybdenum in the inhibition of pitting corrosion in stainless steels, Corrosion Science. 43 (2001) 485-513.

[30] M.H. Moayed, R.C. Newman, Evolution of current transients and morphology of metastable and stable pitting on stainless steel near the critical pitting temperature, Corrosion Science. 48 (2006) 1004-1018.

[31] K. Sasaki, G.T. Burstein, The generation of surface roughness during slurry erosion-corrosion and its effect on the pitting potential, Corrosion Science. 38 (1996) 2111-2120.

[32] L. Peguet, B. Malki, B. Baroux, Influence of cold working on the pitting corrosion resistance of stainless steels, Corrosion Science. 49 (2007) 1933-1948.

[33] S.G. Acharyya, A. Khandelwal, V. Kain, A. Kumar, I. Samajdar, Surface working of 304L stainless steel: Impact on microstructure, electrochemical behavior and SCC resistance, Materials Characterization. 72 (2012) 68-76.

[34] J. Jiang, M.M. Stack, A. Neville, Modelling the tribo-corrosion interaction in aqueous sliding conditions, Tribology International. 35 (2002) 669-679.

Figure Captions

Fig. 1: A schematic diagram showing the tribo-electrochemical cell and test setup.

Fig. 2: Anodic polarization curves measured under sliding and without sliding for 304 stainless steel in 0.5 M NaCl. Test condition: potential sweep rate = 1 mV s^{-1}; sliding contact frequency = 2 Hz; contact load = 10 N.

Fig. 3: SEM image showing the morphology of the sliding track produced during anodic polarization up to 600 mV(SCE). Test condition: same as Fig. 1. Note the existence of corrosion pits inside the sliding track.

Fig. 4: (a) Current transients recorded during sliding at 70 mV(SCE), at various contact frequencies (f) under a contact load of 10 N for 3600 sliding cycles; (b) Total material loss (TML) as a function of total charge measured during sliding at various contact frequencies. The TML measured at the cathodic potential of -900 mV(SCE) is also included in (b) for comparison purpose.

Fig. 5: (a) Three dimensional view of the sliding track and the measured surface profile across the sliding track produced under a contact load of 10 N for 3600 sliding cycles at a potential of 70 mV(SCE) and sliding frequency of 1 Hz. (b) The corresponding wear scar on the alumina counterface.

Fig. 6: Microscopic images showing the sliding tracks produced at various contact frequencies under a contact load of 10 N for 3600 sliding cycles. Potential: 70 mV(SCE).

Fig. 7: Current transients recorded during sliding for various durations (a) and variation of total material loss with sliding time (b), at a contact frequency of 2 Hz and under a contact load of 10 N. Potential: 70 mV(SCE).

Fig. 8: Microscopic images showing the sliding tracks produced after various sliding times at a contact frequency of 2 Hz and under a contact load of 10 N. Potential: 70 mV(SCE).

Fig. 9: (a) Current transients recorded at70 mV(SCE) during sliding under various contact loads at a contact frequency of 2 Hz for 3600 sliding cycles; (b) Variation of total material loss with total charge produced under various contact loads.

Fig. 10: Microscopic images showing the sliding tracks produced under various contact loads at a contact frequency of 2 Hz for 3600 sliding cycles. Potential: 70 mV(SCE).

Fig. 11: AFM images showing (a) the collapse of material into a subsurface pit; (b) a shallow micropit with the pit cover removed by the wear actions; (c) a topography line scan across the micropit and (d) depth profile of the pit shown in (c). Test condition: 70 mV(SCE), 2 Hz, 15 N, 3600 cycles.

Fig. 12: Cross sectional view of the sliding track produced at 1 Hz and 10 N load, showing the micropits at the surface and subsurface (arrowed).

Fig. 13: Three dimensional view of the micropits (a) and a sectional view of a large pit (b) along the dashed line in (a). Test condition: 70 mV(SCE), 1 Hz, 10 N, 3600 cycles.

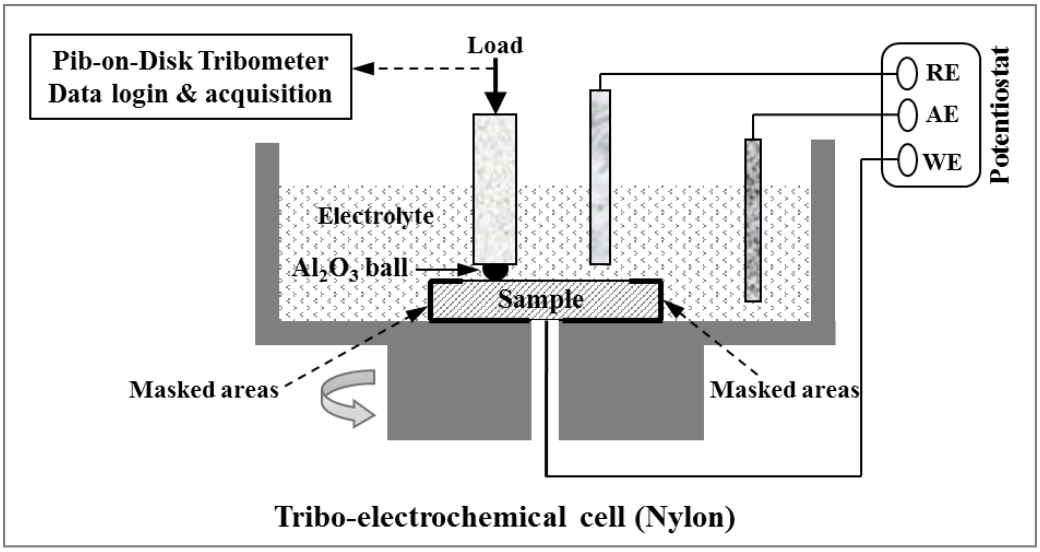

Fig. 1: A schematic diagram showing the tribo-electrochemical cell and test setup.

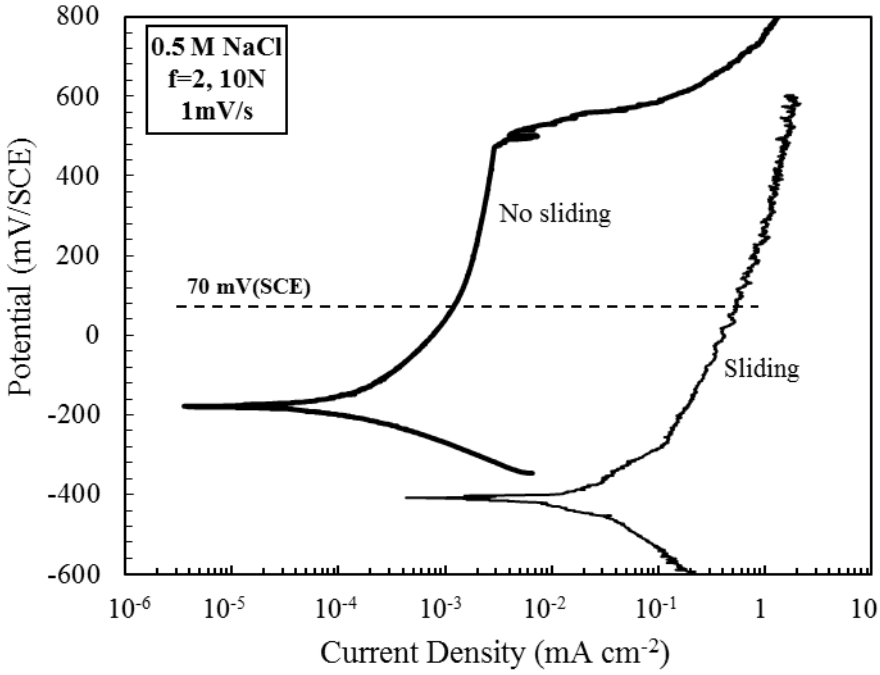

Fig. 2: Anodic polarization curves measured under sliding and without sliding for 304 stainless steel in 0.5 M NaCl. Test condition: potential sweep rate = 1 mV s^{-1}; sliding contact frequency = 2 Hz; contact load = 10 N.

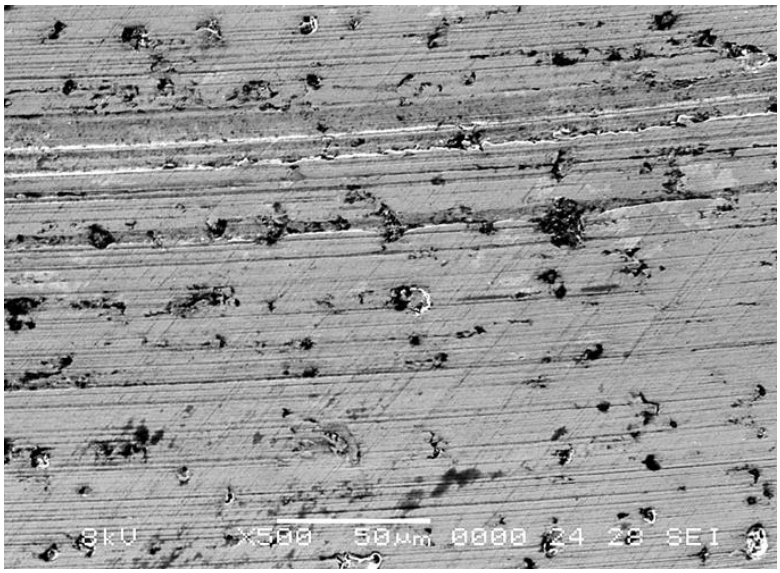

Fig. 3: SEM image showing the morphology of the sliding track produced during anodic polarization up to 600 mV(SCE). Test condition: same as Fig. 1. Note the existence of corrosion pits inside the sliding track.

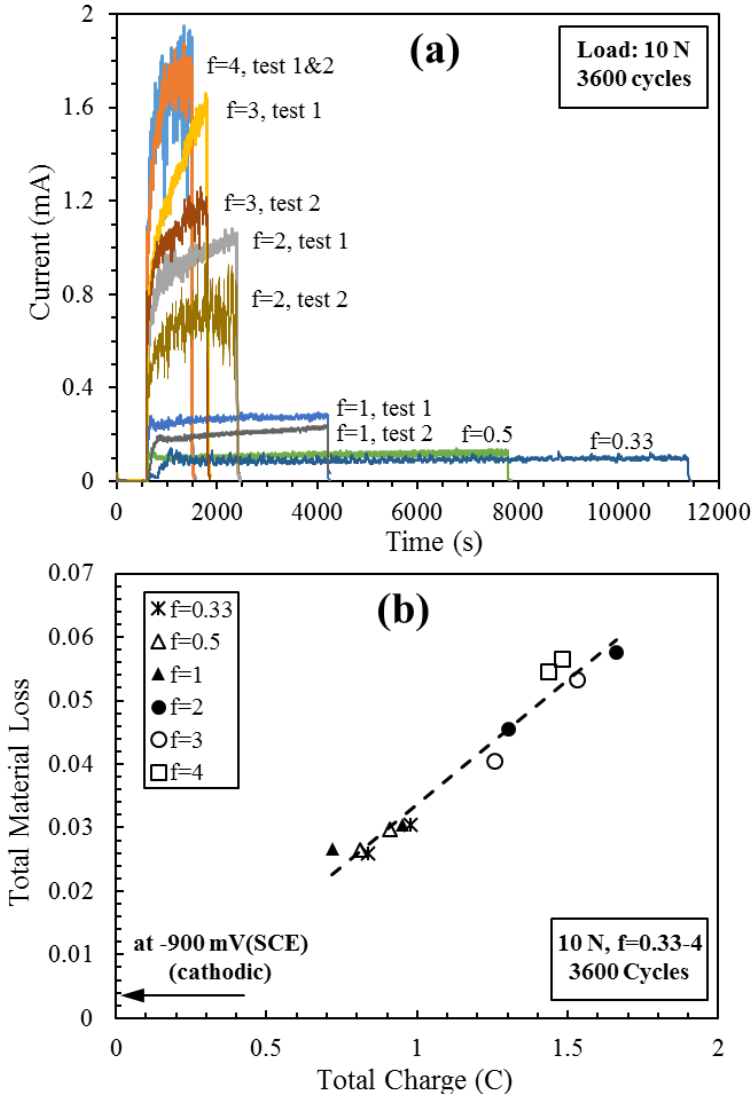

Fig. 4: (a) Current transients recorded during sliding at 70 mV(SCE), at various contact frequencies (f) under a contact load of 10 N for 3600 sliding cycles; (b) Total material loss (TML) as a function of total charge measured during sliding at various contact frequencies. The TML measured at the cathodic potential of -900 mV(SCE) is also included in (b) for comparison purpose.

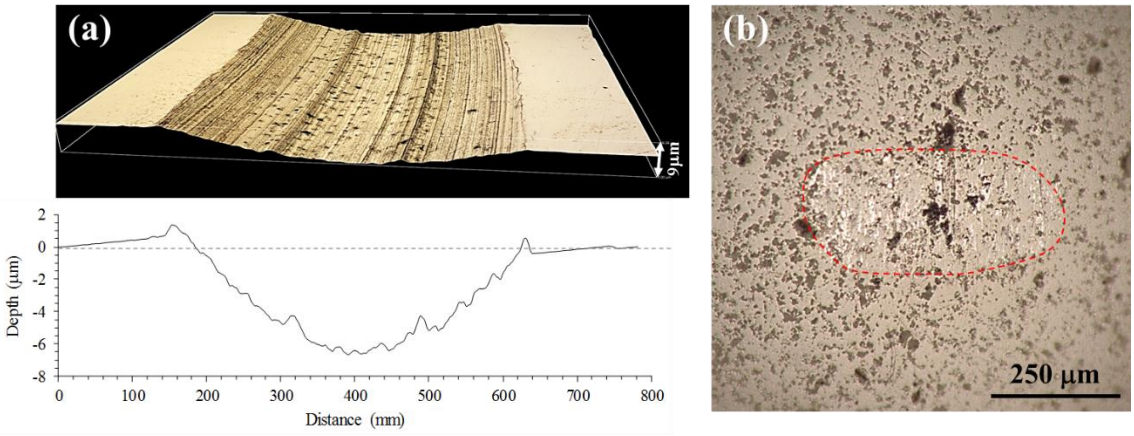

Fig. 5: (a) Three dimensional view of the sliding track and the measured surface profile across the sliding track produced under a contact load of 10 N for 3600 sliding cycles at a potential of 70 mV(SCE) and sliding frequency of 1 Hz. (b) The corresponding wear scar on the alumina counterface.

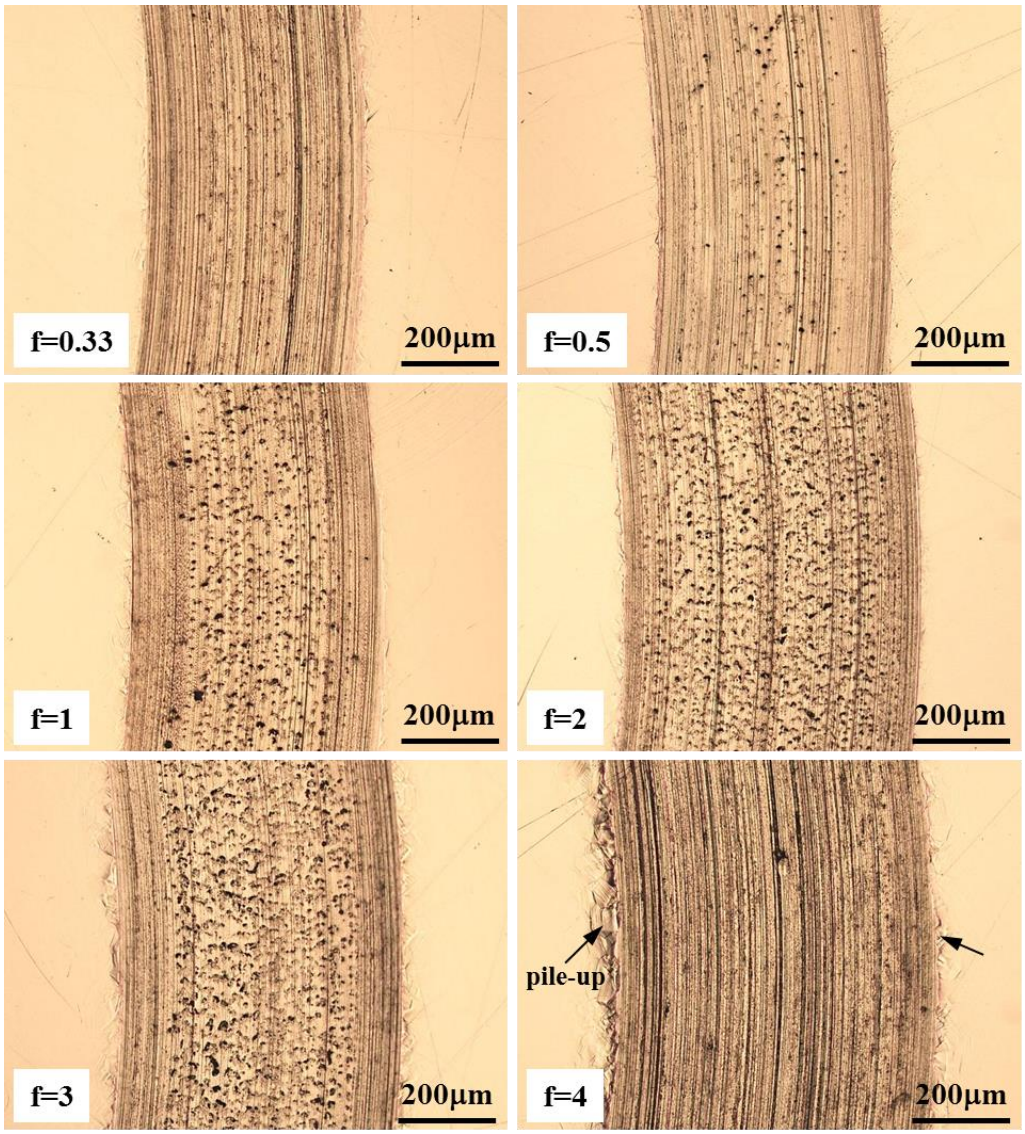

Fig. 6: Microscopic images showing the sliding tracks produced at various contact frequencies under a contact load of 10 N for 3600 sliding cycles. Potential: 70 mV(SCE).

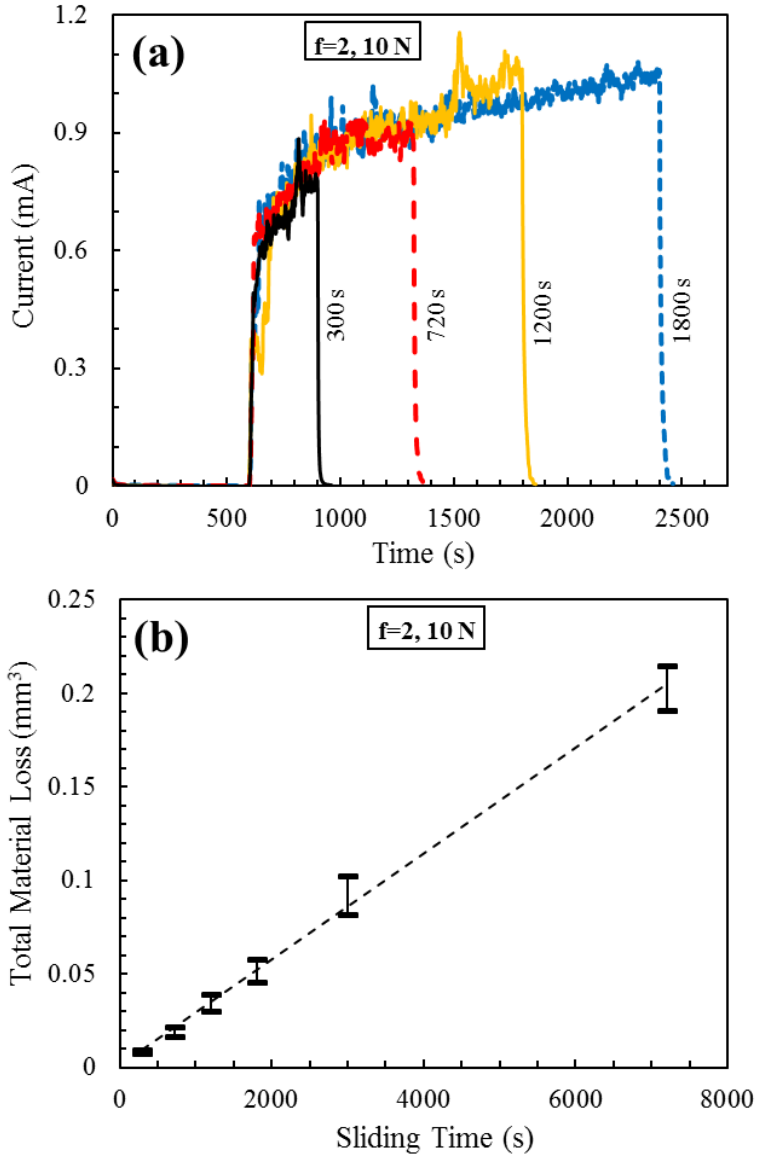

Fig. 7: Current transients recorded during sliding for various durations (a) and variation of total material loss with sliding time (b), at a contact frequency of 2 Hz and under a contact load of 10 N. Potential: 70 mV(SCE).

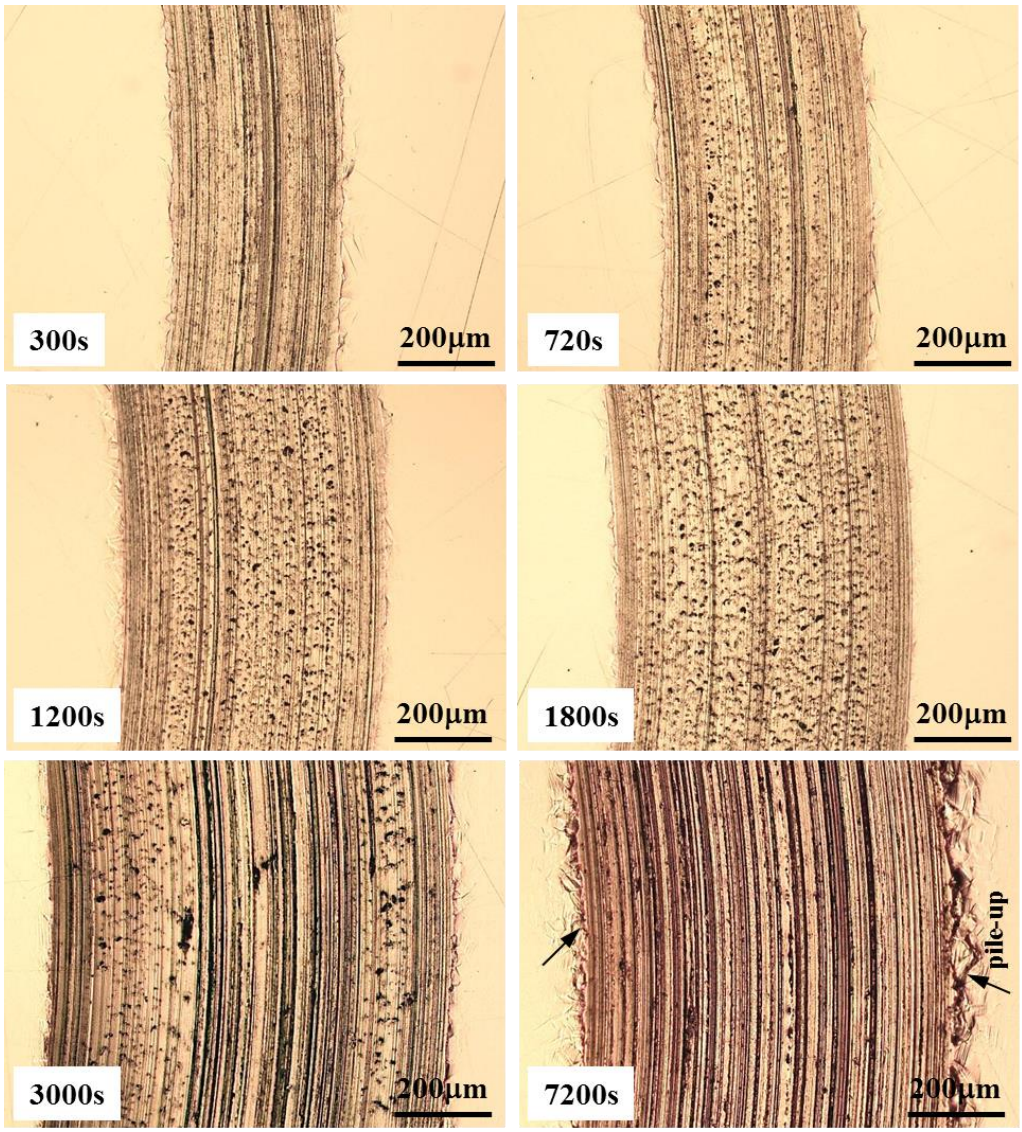

Fig. 8: Microscopic images showing the sliding tracks produced after various sliding times at a contact frequency of 2 Hz and under a contact load of 10 N. Potential: 70 mV(SCE).

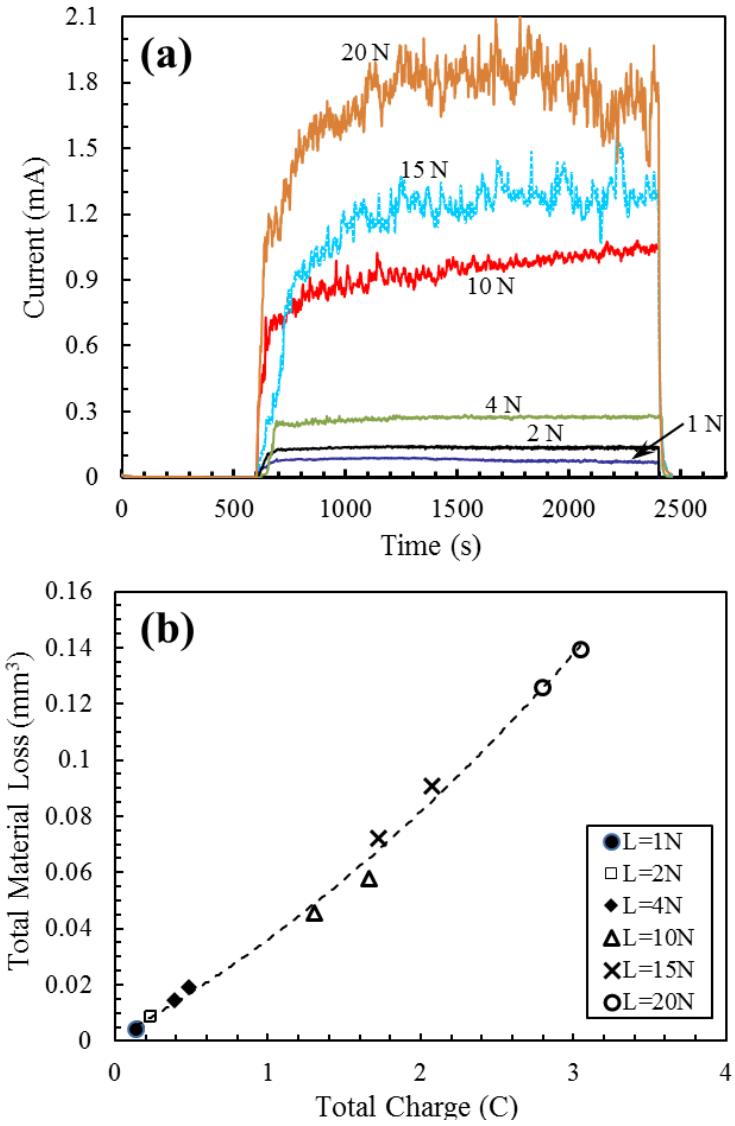

Fig. 9: (a) Current transients recorded at70 mV(SCE) during sliding under various contact loads at a contact frequency of 2 Hz for 3600 sliding cycles; (b) Variation of total material loss with total charge produced under various contact loads.

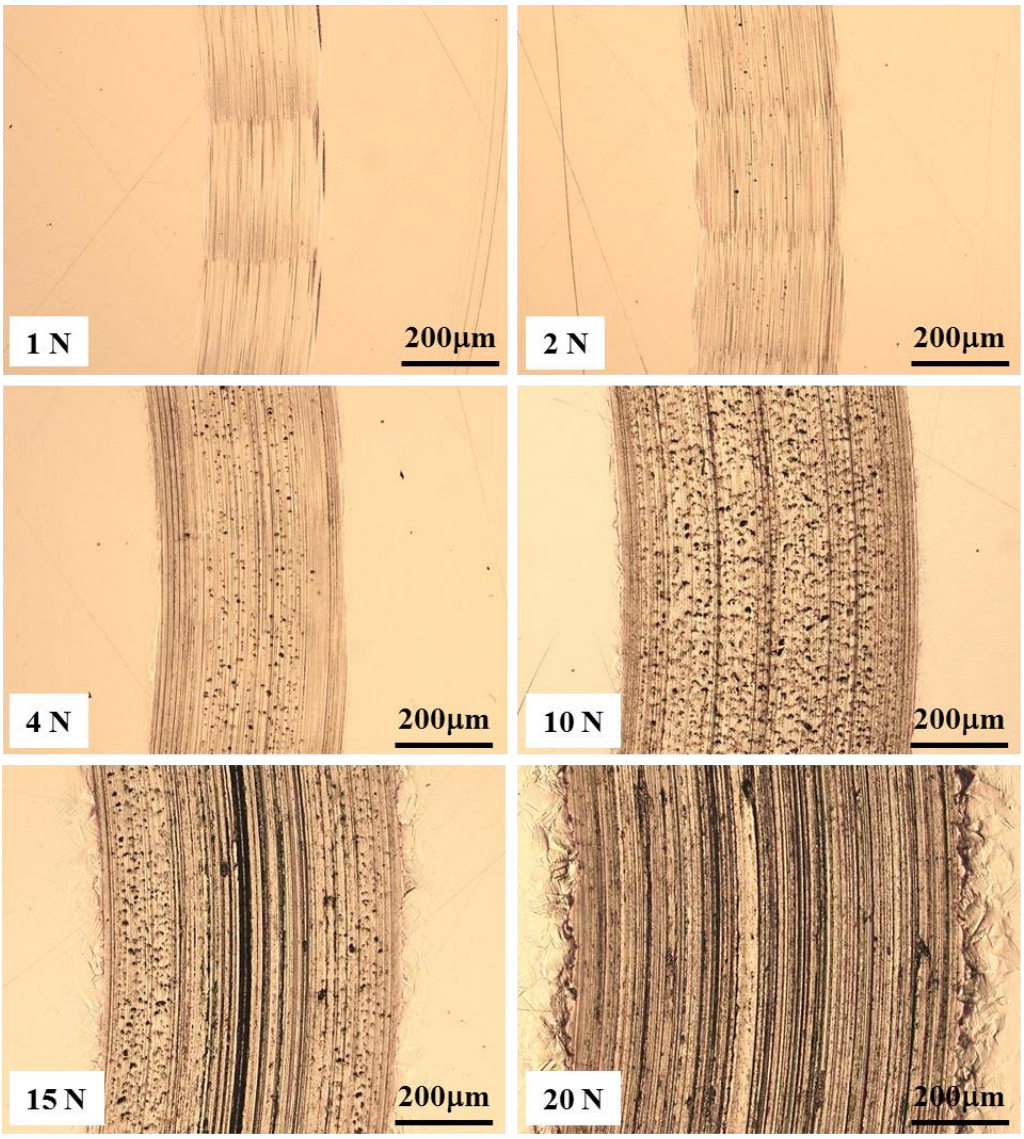

Fig. 10: Microscopic images showing the sliding tracks produced under various contact loads at a contact frequency of 2 Hz for 3600 sliding cycles. Potential: 70 mV(SCE).

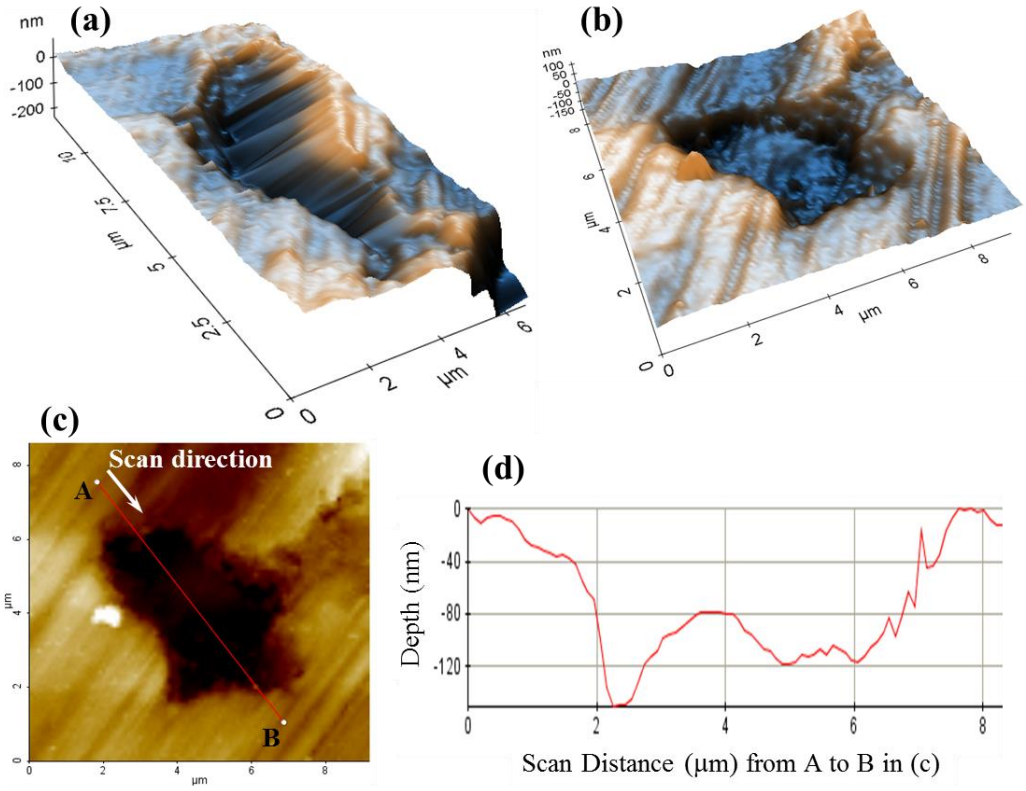

Fig. 11: AFM images showing (a) the collapse of material into a subsurface pit; (b) a shallow micropit with the pit cover removed by the wear actions; (c) a topography line scan across the micropit and (d) depth profile of the pit shown in (c). Test condition: 70 mV(SCE), 2 Hz, 15 N, 3600 cycles.

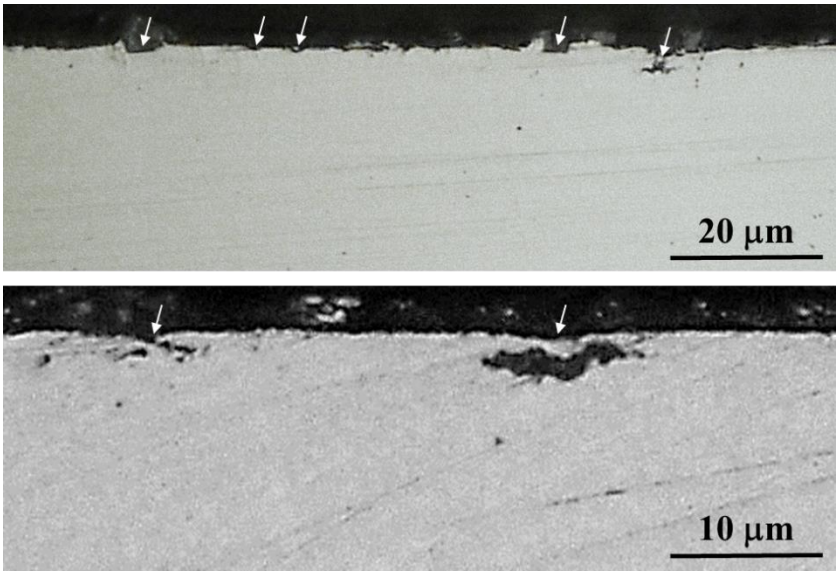

Fig. 12: Cross sectional view of the sliding track produced at 1 Hz and 10 N load, showing the micropits at the surface and subsurface (arrowed).

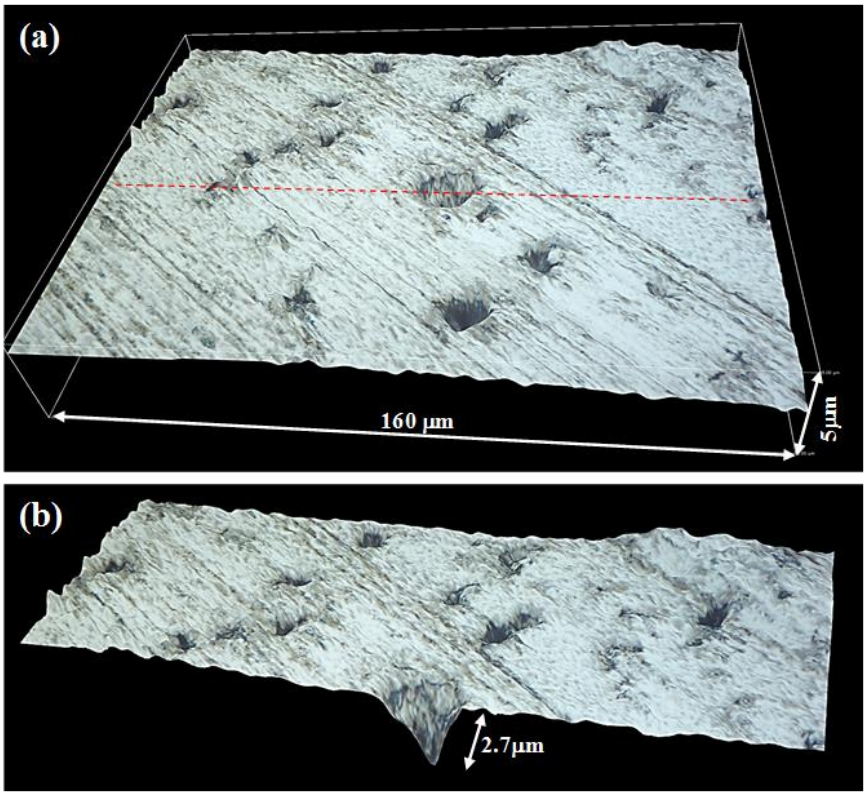

Fig. 13: Three dimensional view of the micropits (a) and a sectional view of a large pit (b) along the dashed line in (a). Test condition: 70 mV(SCE), 1 Hz, 10 N, 3600 cycles.